Hybrid Flush and Synthetic Air Data Filter for Entry Vehicle Atmospheric State Estimation

Christopher D. Karlgaard*
Analytical Mechanics Associates, Inc., Hampton, VA, 23666

A hybrid flush/synthetic air data sensing filter utilizing Kalman-Schmidt and Rach-Tung-Striebel smoothers is developed to obtain entry vehicle atmosphere estimates.The filter/smoother blends information from pressure sensors distributed on the heatshield with measurements of the vehicle aerodynamic forces and moments computed from mass properties and inertial measurement unit data, and prior estimates of the atmosphere. The filter produces estimates of the atmospheric conditions along the entry trajectory, and systematic error estimates to reconcile differences between the pressure and aerodynamic data sources. The filter is applied to data acquired during the Mars Science Laboratory and Mars 2020 entry, descent, and landing at Gale crater and at Jezero crater, respectively. The results show that the hybrid filter produces estimates of the freestream flight condition with lower uncertainty than either the flush or synthetic air data algorithms. The filter accomplishes this result by incorporating additional data and computing estimates of systematic error parameters in the pressure data and the aerodynamic model to further reduce the uncertainties.

Nomenclature

$\boldsymbol{a}$	=	Acceleration, m/s^2
b	=	Reference length, m
$\boldsymbol{C}$	=	State-parameter covariance
C_A, C_Y, C_N	=	Axial, side, and normal force coefficients
C_l, C_m, C_n	=	Roll, pitch, and yaw moment coefficients
$\boldsymbol{\mathcal{F}}$	=	Aerodynamic force, N
$\boldsymbol{\mathcal{F}}_{RCS}$	=	Force due to reaction control system, N
$\boldsymbol{f}$	=	Continuous-time process model
$\boldsymbol{G}$	=	Partial derivative of $\boldsymbol{\phi}$ with respect to $\boldsymbol{u}$
g	=	Gravitational acceleration, m/s^2
$\boldsymbol{H}$	=	Partial derivative of $\boldsymbol{h}$ with respect to $\boldsymbol{x}$
$\boldsymbol{H}_a$	=	State-Atmosphere measurement relation matrix
$\boldsymbol{h}$	=	Measurement model
$\boldsymbol{\mathcal{I}}$	=	Inertia, kg-m^2
i	=	Iteration index
$\boldsymbol{K}$	=	Kalman gain
k	=	Time index
$\boldsymbol{L}$	=	Partial derivative of $\boldsymbol{h}$ with respect to $\boldsymbol{u}$
$\boldsymbol{\mathcal{M}}$	=	Aerodynamic moment, N-m
$\boldsymbol{\mathcal{M}}_{RCS}$	=	Moment due to reaction control system, N
$\boldsymbol{M}$	=	Smoothing gain
M	=	Mach number
m	=	Mass, kg
$\boldsymbol{P}$	=	State covariance
$\boldsymbol{p}$	=	Pressure, Pa
p_s	=	Static pressure, Pa
$\boldsymbol{Q}$	=	Process noise spectral density

*Aerospace Engineer, Associate Fellow AIAA.

$\boldsymbol{R}$	=	Measurement noise covariance
r	=	Radius, m
S	=	Reference area, m^2
t	=	Time, s
$\boldsymbol{u}$	=	Filter consider parameters
V_A	=	Wind-relative velocity magnitude, m/s
v_n, v_e, v_d	=	North, east, and down components of velocity, m/s
w_n, w_e, w_d	=	North, east, and down components of wind, m/s
$\boldsymbol{x}$	=	Filter state
$\boldsymbol{y}$	=	Filter measurements
α	=	Angle of attack, rad
α_T	=	Total angle of attack, rad
β	=	Angle of sideslip, rad
Δt	=	Time step, s
$\boldsymbol{\zeta}$	=	Systematic error states
$\boldsymbol{\eta}$	=	Process noise
Θ	=	Longitude, rad
θ	=	Pitch angle, rad
Λ	=	Declination, rad
$\boldsymbol{\lambda}$	=	Aerodynamic database uncertainty factors
$\boldsymbol{\nu}$	=	Navigation state
ρ	=	Density, kg/m^3
$\boldsymbol{\Phi}$	=	State transition matrix, partial derivative of $\boldsymbol{\phi}$ with respect to $\boldsymbol{x}$
$\boldsymbol{\phi}$	=	Discrete-time process model
φ	=	Roll angle, rad
ψ	=	Yaw angle, rad
$\boldsymbol{\Omega}$	=	Covariance of $\boldsymbol{u}$
$\boldsymbol{\omega}$	=	Angular velocity, rad/s

I. Introduction

Reconstruction of as-flown atmospheres is an important part of the post-flight data analysis of planetary Entry, Descent, and Landing (EDL). The reconstruction is of scientific interest for providing in-situ measurements of the atmoto refine atmospheric modeling and ultimately to inform future missions and potentially improve key metrics such as landing errors.

Reconstruction of planetary entry trajectories at Earth benefit from satellite observations and weather balloon data, but there is a sparser set of observations available at other planets. The typical approach for characterizing the as-flown atmosphere at planets other than Earth assumes that the vehicle aerodynamics are known, and the nominal aerodynamic force coefficients are used on conjunction with measured accelerations from the on-board Inertial Measurement Unit (IMU) and navigation state estimates to solve for the freestream atmosphere and atmospheric relative trajectory. A history and details of the methodology of this approach for entry vehicle atmosphere estimation is given in [1].

The approach described in [1] has the drawback that any errors in the nominal aerodynamic model are injected directly into the estimates of the freestream atmosphere. Errors in the aerodynamic models, in particular those based on Computational Fluid Dynamics (CFD) solutions, often arise due to integration of the pressure distribution across areas on the forebody where the flow physics is not well understood, such as near the shoulder where the forebody interfaces with the backshell, backshell geometry, flow chemistry, and leeside areas for lifting capsule configurations.

Flush Air Data Sensing (FADS) systems have been developed in which a number of pressure ports are installed in the vehicle forebody to directly measure the pressure distribution. These ports can be located at areas where there is confidence in the ability of computational and/or experimental models to predict the pressures based on known freestream conditions. Thus, errors due to modeling uncertainties can be mitigated. Literature reviews on the application of the FADS approach for entry vehicle state estimation are described in [2–4]. Real-time FADS data processing has been demonstrated for aircraft applications with a pilot in the loop in [5], and for sharp-nosed automated hypersonic aircraft in [6]. Proposed real-time sharp-nosed FADS algorithms have been explored in [7]. To date, FADS applications to blunt-body entry vehicles have been limited to post-flight evaluation of the trajectory. Simulation studies have

indicated benefits of the use of FADS in real-time guidance for planetary entry [8]. Navigation system performance studies with FADS have been presented in [9, 10].

One drawback to FADS is that the system requires additional sensors and other supporting electronics, which are subject to the possibility of hardware failure. These failures can lead to corrupt air data estimates [11]. One mitigation approach is to develop a sensor fault detection algorithm to isolate and remove corrupted measurement data [12–15]. Another mitigation approach is to develop backup systems that can be used in the event of total air data system failure. Typically these approaches rely on a filter approach leveraging an aerodynamic model of the aircraft to compute estimates of the atmospheric-relative state. One such approach was termed the Synthetic Air Data System (SADS) [16], where an aerodynamic model of an aircraft is fused with inertial navigation and global positioning system data in a Kalman filter to estimate the freestream conditions. The approach was developed as a back-up for a traditional aircraft air data sensing system, or as a potential low-cost primary system for small robotic aerial vehicles. A frequency domain approach was explored in [17] and application to fighter aircraft air data estimation using a neural network approach was explored in [18].

The SADS approach was extended to the problem of entry vehicle atmospheric state estimation in [19]. A Kalman-Schmidt filter framework was implemented to process data from aerodynamic force and moment pseudo-measurements to compute estimates of the atmospheric state along the trajectory. These force and moment pseudo-measurements were computed based on vehicle mass properties and the linear acceleration and angular rate outputs from an on-board IMU. The proposed method was tested against measured flight data from the Mars Science Laboratory (MSL) Entry, Descent, and Landing Instrumentation (MEDLI) sensors, which included an array of seven pressure ports installed in the heatshield configured as a FADS system [2]. Results from the SADS filter were in reasonable agreement to those computed from the FADS measurements, though with higher uncertainties than the FADS results. The SADS approach was also applied to data from the Mars Phoenix and InSight atmospheric entries [20], which were not instrumented with FADS systems. The SADS results were compared to those of the classical aerodatabase (ADB) reconstruction [1]. The results indicated that the SADS method can produce estimates of the atmosphere with lower uncertainties than the classical ADB method, and furthermore can provide estimates the atmospheric winds.

Model-aided air data estimation approaches have also been investigated in [21–25]. These methods blend synthetic air data with various air data sensors such as pitot-static tubes or air flow vanes to produce estimates of the atmospheric-relative trajectory, in a variety of filter frameworks. The model-aided approaches provide redundancy for air data sensors in a single unified filter architecture by providing aircraft model data to fill in any information that is not provided by the flow sensors. The use of pitot-static tubes and air flow vanes are, however, not suitable for high speed applications such as atmospheric entry due to the aeroheating environments.

This paper describes the development of a hybrid approach in which both FADS pressure measurements and an aerodynamic model are combined in a single filter to estimate the freestream atmospheric-relative state of an entry vehicle. In this approach, the FADS measurements and SADS pseudo-measurements are processed jointly in the filter framework. This approach offers redundancy similar to the model-aided estimation approaches mentioned above and is suitable for entry vehicle or other high speed flight applications.

The remainder of this paper is organized as follows. Section II described the formulation of the proposed hybrid filter, which include measurements models and the FADS, SADS, and prior atmosphere estimate. A simplified process model based on the hydrostatic equilibrium equation and the ideal gas law is implemented for propagating state estimates through time. The proposed filter is applied to data from MSL and Mars 2020 EDL in Section III including as overview of the available data sources and results of the filter implementation. Concluding remarks are given in Section IV.

II. Hybrid Filter Formulation

This section describes the formulation of the proposed hybrid FADS/SADS atmosphere estimation filter. The approach combines estimates of the navigation state of the vehicle with FADS pressure measurements, SADS force and moment pseudo-measurements, and prior estimates of the atmosphere to produce a combined estimate of the atmospheric state along the vehicle flight path.

In the following sections, the filter state is defined as

$$\boldsymbol{x} = [\rho, p_s, w_n, w_e, w_d, \boldsymbol{\zeta}]^\intercal \tag{1}$$

where $\boldsymbol{\zeta}$ are systematic error parameters to be estimated as filter states. These parameters are discussed in the following section.

The navigation state of the vehicle is defined as

$$\boldsymbol{\nu} = [r, \Theta, \Lambda, v_n, v_e, v_d, \varphi, \theta, \psi]^\intercal \tag{2}$$

Parameters consisting of the combination navigation state and aerodynamic parameters that are not estimated as filter states (denoted as $\boldsymbol{\lambda}$) are modeled as consider parameters, given by $\boldsymbol{u} = [\boldsymbol{\nu}, \boldsymbol{\lambda}]^\intercal$. These parameters have uncertainties described as zero mean with covariance $\boldsymbol{\Omega}$ that is considered in the filter weighting and uncertainty estimates.

A. Measurement Model

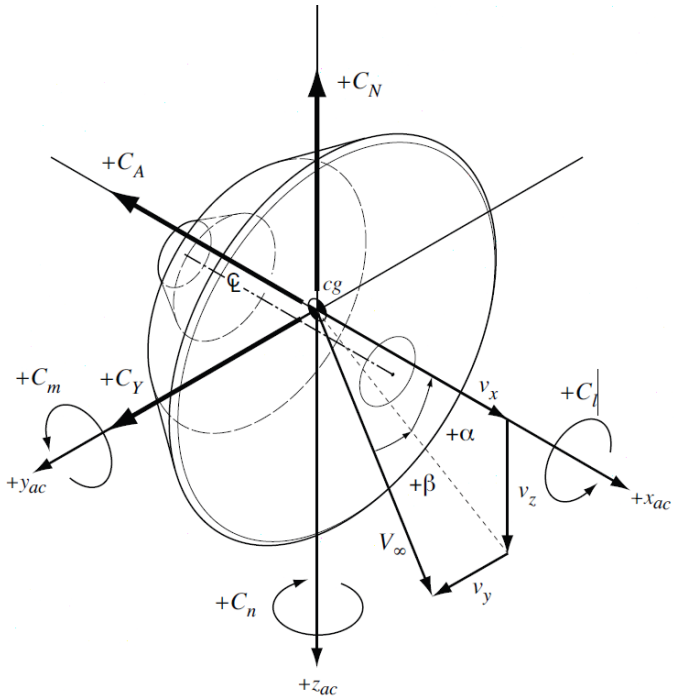

Fig. 1 Aerodynamic Coordinate Frame Definition.

The measurements to be processed in the hybrid filter formulation include FADS pressure measurements, aerodynamic force and moment pseudo-measurements, and prior predictions of the atmosphere along the trajectory.

1. Flush Air Data Sensing

FADS pressure models are typically based on analytical potential [26] or Newtonian flow theories [27], and can include correction factors based on experimental [28] and/or numerical [29] data. Alternately, the model can be based on tabulated CFD solutions [2–4, 30]. In any case, the pressure model can be written as a function of the atmosphere and model parameters as $\boldsymbol{p} = \boldsymbol{p}(\boldsymbol{x}, \boldsymbol{u})$. Components of the state $\boldsymbol{\zeta}$ can include systematic error parameters such as multiplicative (scale factor) and additive (bias) errors to be estimated in the filter.

2. Synthetic Air Data Sensing

The aerodynamic force and moment acting on the vehicle can be computed from the IMU measurements of acceleration, $\boldsymbol{a}$ (after transformation from the IMU location to the vehicle center of mass), and angular rate, $\boldsymbol{\omega}$. The force and moment predictive model is based on an aerodynamic database that relates the force and moment coefficients (shown in Fig. 1) to the atmosphere and trajectory state. The force and moment equations are

$$\boldsymbol{\mathcal{F}}(\boldsymbol{x},\boldsymbol{u}) = m\boldsymbol{a} - \boldsymbol{\mathcal{F}}_{RCS} = \frac{\rho V_A^2 S}{2}\left\{\begin{array}{c} -C_A(\alpha,\beta,M,\boldsymbol{\zeta},\boldsymbol{\lambda}) \\ C_Y(\alpha,\beta,M,\boldsymbol{\zeta},\boldsymbol{\lambda}) \\ -C_Z(\alpha,\beta,M,\boldsymbol{\zeta},\boldsymbol{\lambda}) \end{array}\right\} \tag{3}$$

$$\boldsymbol{\mathcal{M}}(\boldsymbol{x},\boldsymbol{u}) = \boldsymbol{\mathcal{I}}\dot{\boldsymbol{\omega}} + \boldsymbol{\omega}\times\boldsymbol{\mathcal{I}}\boldsymbol{\omega} - \boldsymbol{\mathcal{M}}_{RCS} = \frac{\rho V_A^2 S b}{2}\left\{\begin{array}{c} C_l(\alpha,\beta,M,\boldsymbol{\zeta},\boldsymbol{\lambda}) \\ C_m(\alpha,\beta,M,\boldsymbol{\zeta},\boldsymbol{\lambda}) \\ C_n(\alpha,\beta,M,\boldsymbol{\zeta},\boldsymbol{\lambda}) \end{array}\right\} \tag{4}$$

Note that the Mach Number, $M(\boldsymbol{x},\boldsymbol{u})$, and flow angles, $\alpha(\boldsymbol{x},\boldsymbol{u})$ and $\beta(\boldsymbol{x},\boldsymbol{u})$, are functions of the atmospheric state and the navigation state. The aerodynamic flow angles are shown in Fig. 1.

The components of the state corresponding to $\boldsymbol{\zeta}$ consist of systematic error parameters such as multiplicative and additive constants that are used to adjust the force and moment coefficients to fit the measurement data. The parameters λ are other aerodynamic terms that are uncertain but are not estimated in the filter.

3. Atmosphere

Prior estimates of atmosphere conditions along the trajectory can be tabulated as a function of the position and time. These data provide an initial reference for the atmospheric conditions. The relation between the measurement and the state is $\boldsymbol{H}_a\boldsymbol{x}$ where $\boldsymbol{H}_a = \left[\begin{array}{cc} \boldsymbol{I} & \boldsymbol{0} \end{array}\right]$, where $\boldsymbol{I}$ here is a 5x5 identity matrix, and $\boldsymbol{0}$ is a zero matrix with 5 rows and length($\boldsymbol{\zeta}$) columns.

4. Combined Measurement Model

Assembling the pressure, aerodynamics, and atmosphere measurements, the resulting model is

$$\boldsymbol{y} = \boldsymbol{h}(\boldsymbol{x},\boldsymbol{u}) = \left\{\begin{array}{c} \boldsymbol{p}(\boldsymbol{x},\boldsymbol{u}) \\ \boldsymbol{\mathcal{F}}(\boldsymbol{x},\boldsymbol{u}) \\ \boldsymbol{\mathcal{M}}(\boldsymbol{x},\boldsymbol{u}) \\ \boldsymbol{H}_a\boldsymbol{x} \end{array}\right\} \tag{5}$$

Partial derivatives of $\boldsymbol{h}$ with respect to $\boldsymbol{x}$ and $\boldsymbol{u}$ are defined as $\boldsymbol{H} = (\partial\boldsymbol{h}/\partial\boldsymbol{x})$ and $\boldsymbol{L} = (\partial\boldsymbol{h}/\partial\boldsymbol{u})$.

B. Process Model

Following [3, 19, 20], a reasonable simplified process model relating to the change in atmosphere along the trajectory can be formulated based on the hydrostatic equation and assuming a random walk for the rate of change of temperature and winds. Similarly the systematic error states can be modeled as a random walk process. The process model takes the form

$$\dot{\boldsymbol{x}} = \boldsymbol{f}(\boldsymbol{x},\boldsymbol{u}) + \boldsymbol{\eta} \tag{6}$$

where

$$\boldsymbol{f}(\boldsymbol{x},\boldsymbol{u}) = g(r,\Theta,\Lambda)\,\rho v_d\left\{\begin{array}{c} \rho/p_s \\ 1 \\ \boldsymbol{0} \end{array}\right\} \tag{7}$$

where $\boldsymbol{0}$ here is a zero row vector of length 3+length($\boldsymbol{\zeta}$). The continuous process model can be written in discrete form as

$$\boldsymbol{x}_{k+1} = \boldsymbol{\phi}(\boldsymbol{x}_k,\boldsymbol{u}_k) = \boldsymbol{x}_k + \boldsymbol{f}(\boldsymbol{x}_k,\boldsymbol{u}_k)\,\Delta t \tag{8}$$

Partial derivatives of $\boldsymbol{\phi}$ with respect to $\boldsymbol{x}$ and $\boldsymbol{u}$ are defined as $\boldsymbol{\Phi} = (\partial\boldsymbol{\phi}/\partial\boldsymbol{x})$ and $\boldsymbol{G} = (\partial\boldsymbol{\phi}/\partial\boldsymbol{u})$.

C. Estimator Formulation

The hybrid estimation approach is based on an Iterative Extended Kalman-Schmidt Filter (IEKSF) [31] that runs forward through the dataset, and a Rauch-Tung-Streibel (RTS) smoother [32] that runs backwards through the data after the forward pass. Estimates of the state are denoted by $\hat{\boldsymbol{x}}_{k|m}$, meaning the estimate at time k conditioned on data through time m. The case of $k > m$ is known as prediction, $k = m$ is filtering, and $k < m$ is smoothing. Similarly, the state error covariance is $\hat{\boldsymbol{P}}_{k|m}$.

1. Iterative Extended Kalman-Schmidt Filter

Beginning with the filter initial conditions at time $k = 0$, the filter prediction step is given by

$$\hat{\boldsymbol{x}}_{k|k-1} = \boldsymbol{\phi}\left(\hat{\boldsymbol{x}}_{k-1|k-1}, \boldsymbol{u}_{k-1}\right) \tag{9}$$

$$\hat{\boldsymbol{P}}_{k|k-1} = \boldsymbol{\Phi}_{k-1}\hat{\boldsymbol{P}}_{k-1|k-1}\boldsymbol{\Phi}_{k-1}^{\intercal} + \boldsymbol{\Phi}_{k-1}\boldsymbol{C}_{k-1|k-1}\boldsymbol{G}_{k-1}^{\intercal} + \boldsymbol{G}_{k-1}\boldsymbol{C}_{k-1|k-1}\boldsymbol{\Phi}_{k-1}^{\intercal} + \boldsymbol{G}_{k-1}\boldsymbol{\Omega}_{k-1}\boldsymbol{G}_{k-1}^{\intercal} + \boldsymbol{Q}_{k-1} \tag{10}$$

$$\hat{\boldsymbol{C}}_{k|k-1} = \boldsymbol{\Phi}_{k-1}\hat{\boldsymbol{C}}_{k-1|k-1} + \boldsymbol{G}_{k-1}\boldsymbol{\Omega}_{k-1} \tag{11}$$

where $\hat{\boldsymbol{C}}$ is the state-parameter covariance.

Measurements at time k are processed according to the iterative update

$$\boldsymbol{K}_k^i = \hat{\boldsymbol{P}}_{k|k-1}\boldsymbol{H}_k^{i\intercal}\left[\boldsymbol{H}_k^i\hat{\boldsymbol{P}}_{k|k-1}\boldsymbol{H}_k^{i\intercal} + \boldsymbol{H}_k^i\hat{\boldsymbol{C}}_{k|k-1}\boldsymbol{L}_k^{i\intercal} + \boldsymbol{L}_k^i\hat{\boldsymbol{C}}_{k|k-1}\boldsymbol{H}_k^{i\intercal} + \boldsymbol{R}_k\right]^{-1} \tag{12}$$

$$\hat{\boldsymbol{x}}_{k|k}^{i+1} = \hat{\boldsymbol{x}}_{k|k-1} + \boldsymbol{K}_k^i\left[\boldsymbol{y}_k - \boldsymbol{h}\left(\hat{\boldsymbol{x}}_{k|k}^i, \boldsymbol{u}_k\right) - \boldsymbol{H}_k^i\left(\hat{\boldsymbol{x}}_{k|k-1} - \hat{\boldsymbol{x}}_{k|k}^i\right)\right] \tag{13}$$

where the superscript i indicates the iteration index, and $\boldsymbol{K}_k^i$ is the Kalman gain. After convergence, the state and state-parameter covariance are updated as

$$\hat{\boldsymbol{P}}_{k|k} = \left(\boldsymbol{I} - \boldsymbol{K}_k\boldsymbol{H}_k\right)\hat{\boldsymbol{P}}_{k|k-1}\left(\boldsymbol{I} - \boldsymbol{K}_k\boldsymbol{H}_k\right)^{\intercal} + \boldsymbol{K}_k\boldsymbol{R}_k\boldsymbol{K}_k^{\intercal} \tag{14}$$

$$\hat{\boldsymbol{C}}_{k|k} = \hat{\boldsymbol{C}}_{k|k-1} - \boldsymbol{K}_k\left(\boldsymbol{H}_k\hat{\boldsymbol{C}}_{k|k-1} + \boldsymbol{L}_k\boldsymbol{\Omega}_k\right) \tag{15}$$

2. Rauch-Tung-Streibel Smoother

After proessing all n measurements by the forward filter, the information content contained in $\hat{\boldsymbol{x}}_{n|n}$, $\hat{\boldsymbol{P}}_{n|n}$, and $\hat{\boldsymbol{C}}_{n|n}$ can be mapped backward in time to the beginning of the measurements at time index $k = 1$ using the RTS smoother. The smoother initializes at time $k + 1 = n$ and maps the information content back to $k = 1$ using the relations [32]

$$\boldsymbol{M}_k = \hat{\boldsymbol{P}}_{k|k}\boldsymbol{\Phi}_k\hat{\boldsymbol{P}}_{k+1|k}^{-1} \tag{16}$$

$$\hat{\boldsymbol{x}}_{k|n} = \hat{\boldsymbol{x}}_{k|k} + \boldsymbol{M}_k\left(\hat{\boldsymbol{x}}_{k+1|n} - \hat{\boldsymbol{x}}_{k+1|k}\right) \tag{17}$$

$$\hat{\boldsymbol{P}}_{k|n} = \hat{\boldsymbol{P}}_{k|k} + \boldsymbol{M}_k\left(\hat{\boldsymbol{P}}_{k+1|n} - \hat{\boldsymbol{P}}_{k+1|k}\right)\boldsymbol{M}_k^{\intercal} \tag{18}$$

III. Application to the Mars 2020 Entry Atmosphere Reconstruction

The proposed hybrid flush/synthetic air data sensing filter was applied to flight data from the Mars 2020 entry, descent, and landing [33] that occurred on February 18th, 2021. The Mars 2020 capsule was instrumented with sensors to measure the aerodynamic and aerothermodynamic performance of the aeroshell during entry. This sensor system was known as the Mars 2020 Entry, Descent, and Landing Instrumentation (MEDLI2). The sensors included an array of seven pressure ports on the heatshield, arranged as a FADS system for post-flight trajectory and atmosphere reconstruction [4]. The hybrid filter approach was also applied to MSL's MEDLI dataset acquired during Mars EDL on August 6th, 2012. The main results and conclusions drawn from the MEDLI application match with those from the MEDLI2 application, therefore just the MEDLI2 results are shown here for brevity. The remainder of this section provides a summary of the data sources and results of the proposed hybrid filter approach described in this paper.

A. Measurement Data

This section summarizes the data sources from the Mars 2020 entry at Mars that are available for use in the hybrid atmosphere estimation filter. The data sources include the FADS pressure data, aerodynamic forces and moments derived from IMU and mass properties, and an initial atmosphere profile.

1. Pressure Data

The layout of the seven heatshield pressure ports is shown in Fig. 2(a). Note that the Mars 2020 flew a guided, lifting entry, so the stagnation area (in the region of MPH01 and MPH02) is located off the centerline in the pitch plane. Of the seven pressures, one stagnation transducer (MPH01) had a full scale range of 35 kPa to measure pressure across the entire flight range. The other six transducers had a full scale range of 7 kPa. These transducers saturated during the hypersonic flight phase, desaturating prior to supersonic flight to provide high resolution data in that flight regime.

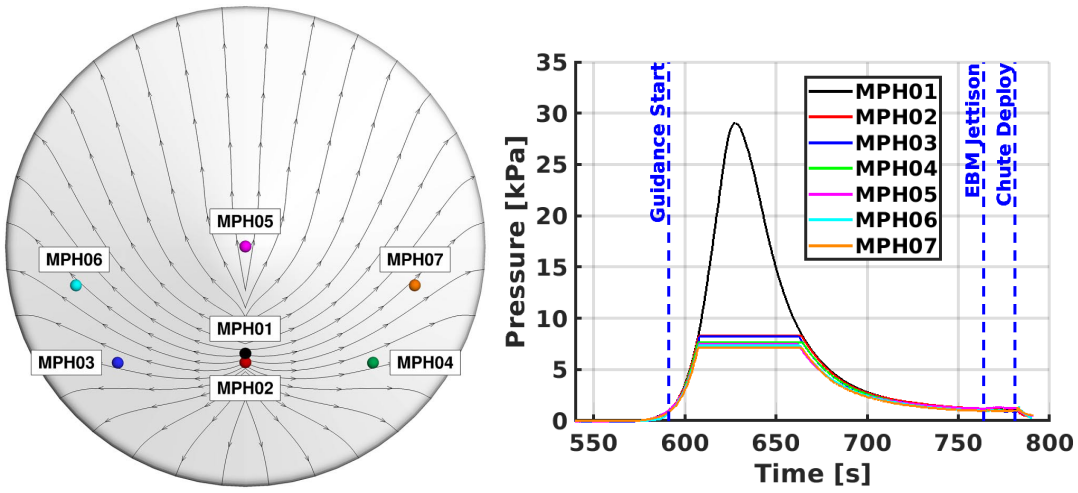

(a) Mars 2020 pressure port layout.

(b) Mars 2020 pressure measurements

Fig. 2 Mars 2020 heatshield pressure ports and measurement data.

The measured pressures during entry are shown in Fig. 2(b). The pressures were sampled at a rate of 8 Hz. Note that the $t = 0$ time corresponds to the on-board guidance start time, which occurred approximately 540 s prior to entry interface. Additional details on the measurement system can be found in [4].

2. Aerodynamic Force and Moment

The on-board IMU sampled linear accelerations and angular rates at a rate of 200 Hz during entry. Raw and filtered IMU data are shown in [4]. The filtered accelerations and rates were used with the mass properties to compute the aerodynamic force and moment acting on the vehicle for use as the synthetic pseudo-measurements. Force and moment due to Reaction Control System (RCS) firings were accounted for based on the commanded RCS firing history and the known jet force and direction.

Examples of the aerodynamics are shown in Fig. 3. This figure shows the pitching moment and axial force constructed from the IMU data and mass properties. The other force and moment axes were constructed for pseudo-measurement processing but are not shown here.

3. Aerodynamic Database

The capsule aerodynamic database provided force and momement coefficients in the coordinate frame shown in Fig. 1. The database consisted of CFD solutions of thin-layer Navier-Stokes equations evaluated along a reference trajectory and tabulated as a function of Mach number, velocity, and total angle of attack. Uncertainties in the aerodynamic database were modeled as a set of additive and multiplicative error terms that can be used to perturb the outputs. These uncertainty inputs were normalized such that a value of zero corresponds to the nominal condition and a value of ± 1 corresponds to a $\pm 3\sigma$ value dispersion. The values of the additive and multiplicate uncertainties are shown in Table 1. Additional details on the aerodynamic database can be found in [34]. Note that the database used in this study includes an updated base pressure model derived from the MEDLI2 backshell pressure transducer data [35] to correct the axial force coefficient in the supersonic flight regime.

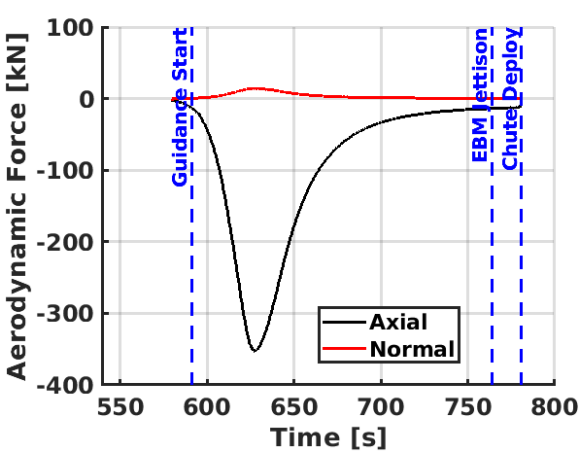

(a) Mars 2020 aerodynamic force.

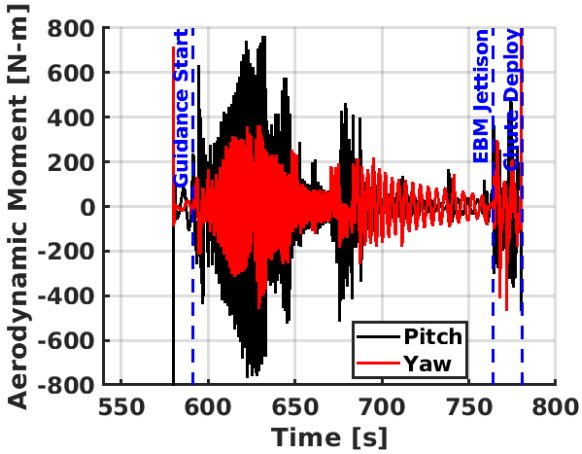

(b) Mars 2020 aerodynamic moment

Fig. 3 Mars 2020 aerodynamics.

Table 1 Aerodynamic uncertainties, 3σ [34].

	C_A	C_N, C_Y	C_m	C_n	C_l
Hypersonic	±3%	±0.01, ±10%	±0.006, ±20%	±0.003, ±20%	±0.000326
Supersonic	±10%	±0.01, ±10%	±0.005, ±20%	±0.005, ±20%	±0.0004

4. Prior Atmosphere Model

Initial atmosphere profiles were constructed as tables evaluated as a function of position along a nominal reference trajectory. These tables provided an initial guess of the atmospheric conditions along the trajectory, which were refined by the filter processing of the pressure and aerodynamic measurements. These data were tabulated from Mars Climate Sounder measurements of the atmosphere near the Mars 2020 landing site [36, 37]. Example data showing the density and pressure are in Fig. 4(a) and the corresponding winds are shown in Fig. 4(b).

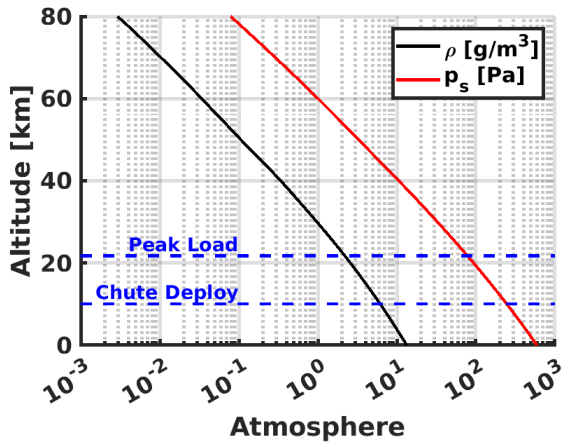

(a) Pressure, density.

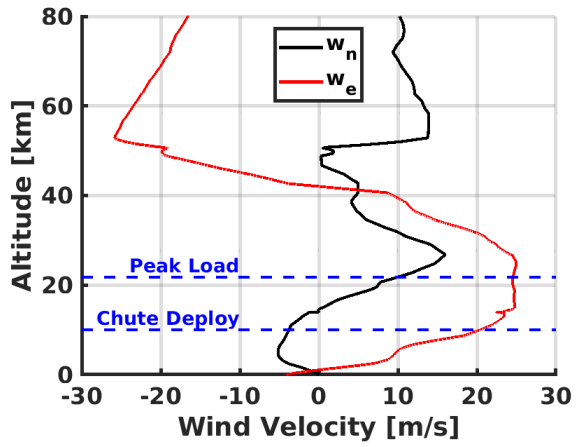

(b) Winds.

Fig. 4 Atmosphere.

B. Filter Results

The results of the application of the hybrid filter approach applied to the Mars 2020 entry data are shown in this section. The hybrid filter is compared to results of the FADS processing from [4] and SADS processing (similar to [19] but for the Mars 2020 application). The filters were initiated at a time of approximately 580 s from the on-board guidance start, or roughly 40 s after entry interface, where there was sufficient signal in the recorded pressures and computed aerodynamics to enable reasonable filter estimates of the atmosphere. The reconstructions were terminated at the time of parachute deployment.

The filter systematic error states included 14 aerodynamic parameters, 7 pressure bias states, and 7 pressure scale factor states. A list of the aerodynamic parameter states can be found in Table 2. These states were modeled in the filter as random constants with an initial 3σ uncertainty of 1. The pressure bias states were modeled as random walk processes with an initial 3σ uncertainty of 1 Pa, assuming an in-flight zero was applied to the data prior to entry interface. The random walk process noise was set to produce a 3σ bias uncertainty of 25 Pa after 200 s. The pressure scale factor states were also modeled as random walk processes with an initial 3σ uncertainty of 0.1% and the random walk process noise was set to create a growth of 0.01% after 200 s. These process noise settings are consistent with thermal calibration and pressure profile testing that shows evidence of hysteresis in the form of a zero drift with a small scale factor thermal sensitivity [38, 39].

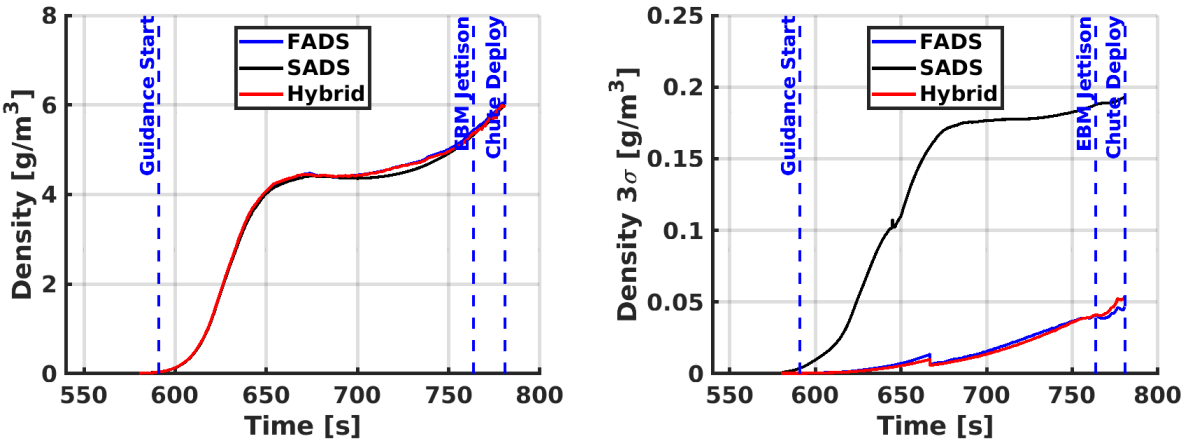

(a) Density.

(b) Density uncertainty.

Fig. 5 Reconstructed density.

Some example results are shown in the following figures. In each case, the FADS result is shown with magenta curves, the SADS results are shown in the black curves, and the new hybrid results are shown in red curves. Fig. 5(a) shows the reconstructed density time history. The estimated values for the three filters follow a similar time history. The density uncertainties shown in Fig. 5(b) shows that the FADS result produces an estimate with smaller uncertainty than the SADS method, which is consistent with the findings from [19]. The hybrid filter result produces an estimate with slightly smaller uncertainty than the FADS solution.

One component of wind, the north wind, is shown in Fig. 6(a) with uncertainties shown in Fig. 6(b). The SADS solution essentially tracks the prior wind profile from Fig. 4(b). Note that the step changes in the wind estimates of the FADS and hybrid filters at the time of approximately 670 s corresponds to the de-saturation of the supersonic range pressure transducers, as shown in Fig. 2(b). Prior to this time, the filters were only processing the single stagnation point pressure measurement and so had reduced sensitivity to winds. In this range the FADS and hybrid filters also tracked the prior wind profile. The SADS method shows slightly lower uncertainties than the FADS filter in this range since the latter was processing a single pressure measurement. The hybrid filter approach has a slightly lower uncertainty than both methods, as expected. After desaturation, the FADS and hybrid filters are more sensitive to the winds since all seven pressure measurements are available for processing and so the estimates are adjusted with higher frequency content, with a corresponding reduction in uncertainties. Following similar trends to the density estimate, the FADS solution after desaturation produces estimates with lower uncertainties than SADS and the hybrid filter further reduces the FADS uncertainties by incorporating additional data and computing estimates of systematic errors. The other components of winds follow a similar trend and so are not shown here.

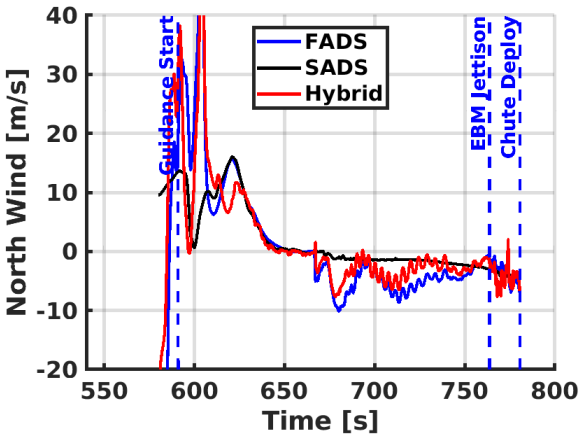

(a) North wind.

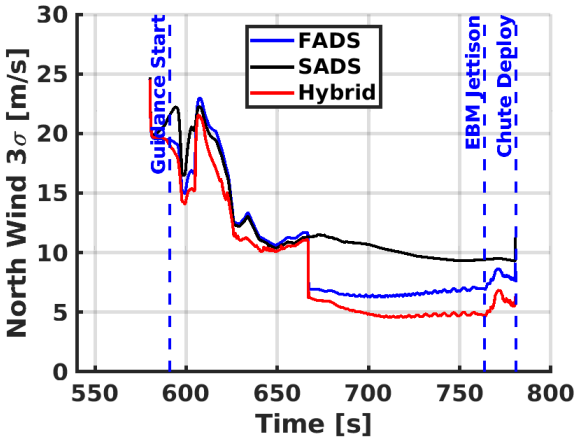

(b) North wind uncertainty.

Fig. 6 Reconstructed north wind.

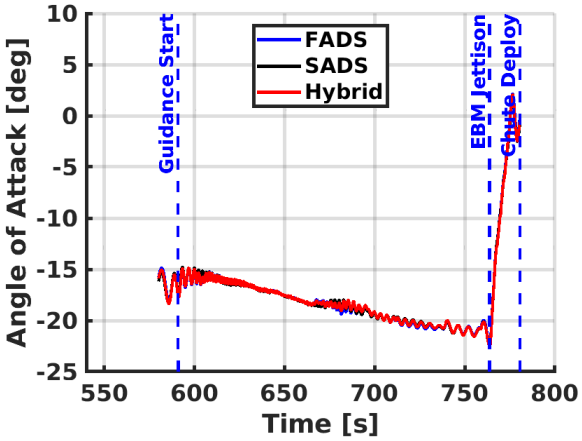

(a) Angle of attack.

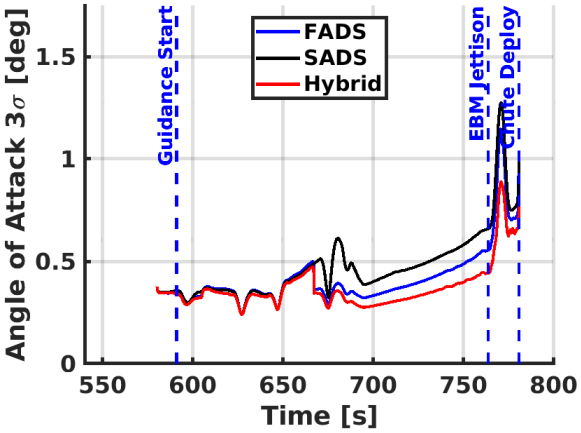

(b) Angle of attack uncertainty.

Fig. 7 Reconstructed angle of attack.

Results similar to the wind reconstruction are reflected in the angle of attack estimates and uncertainties, as shown in Figs. 7(a) and (b), respectively. The angle of attack histories are in agreement between the three results, and the uncertainties are similar in the hypersonic phase of flight where only one FADS pressure port is active. After desaturation of the supersonic pressure transducers, the FADS solution produces smaller uncertainties than the SADS result. The hybrid filter result produces a further reduction in uncertainty by compensating for systematic errors in the pressure measurements. The sideslip angle estimates follow a similar trend and so are not shown here.

Estimates of dynamic pressure and uncertainties are shown in Fig. 8(a) and (b). Here, the SADS result shows a consistently higher uncertainty than the FADS solution, which is consistent with the findings from [19]. The single stagnation pressure measurement in the hypersonic phase provides sufficient data to reconstruct the dynamic pressure with lower uncertainty than the SADS result. The hybrid filter is able to further improve on the FADS solution by both considering the aerodynamic measurements and by compensating for systematic errors. The same trends can be seen in the reconstructed Mach number and uncertainties shown in Fig. 9(a) and (b), respectively.

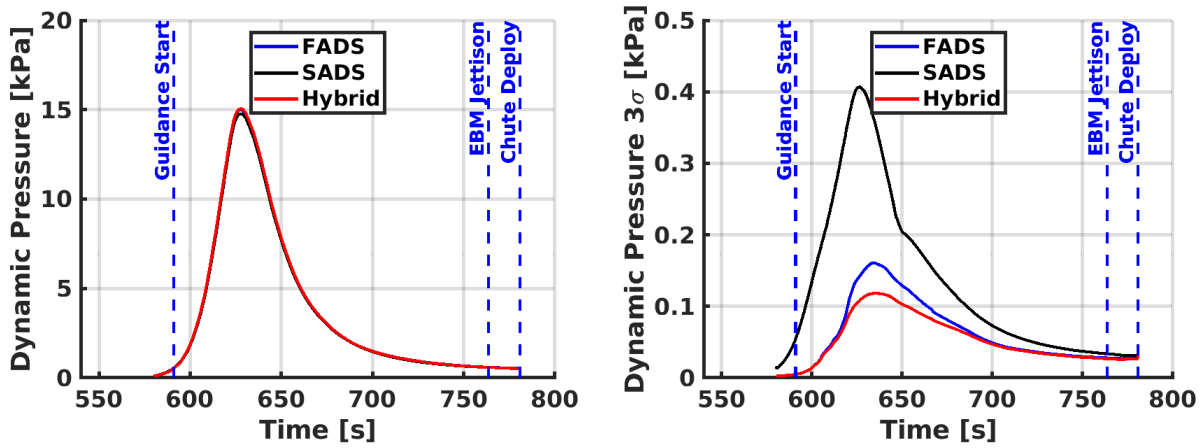

(a) Dynamic pressure.

(b) Dynamic pressure uncertainty.

Fig. 8 Reconstructed dynamic pressure.

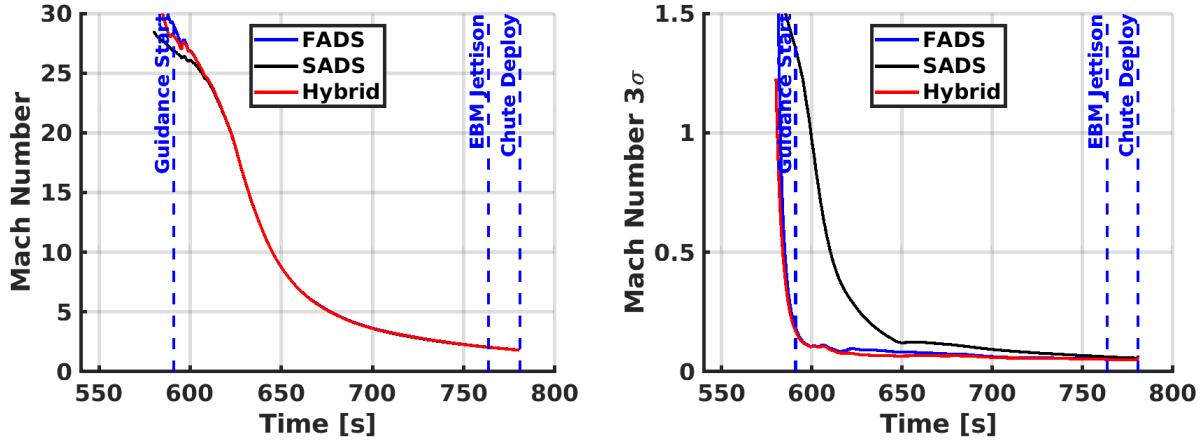

(a) Mach number.

(b) Mach number uncertainty.

Fig. 9 Reconstructed Mach number.

As shown previously, the new hybrid filter is able to produce estimates of the atmospheric-relative trajectory with smaller uncertainties than either the FADS or SADS filters alone. In part, the reduction in uncertainty is accomplished by including systematic error parameters as filter states and thus providing corrections to the measurements. The estimates of the pressure bias states are shown in Fig. 10(a). Recall that these states were modeled as random walk processes that were allowed to vary over the trajectory. The bias uncertainties are shown in Fig. 10(b). Here, the curve labeled FADS corresponds to the uncompensated bias states from the FADS filter solution. The uncompensated bias states reach an uncertainty of approximately 25 Pa at the time of parachute deployment. The hybrid filter is able to reduce the bias uncertainties to under 10 Pa over the entire trajectory.

Results for the scale factor error estimates are shown in Fig. 11(a) with associated uncertainties shown in Fig. 11(b). The curve labeled FADS in Fig. 11(b) corresponds to the uncompensated scale factor uncertainties. The hybrid filter is able to reduce the scale factor uncertainties along the trajectory by solving for these parameters as filter states. Note that the scale factor uncertainties appear close to constant values because these were modeled as random walk processes with a variance smaller relative to the bias errors, which was informed by ground testing of the pressure transducers [38, 39].

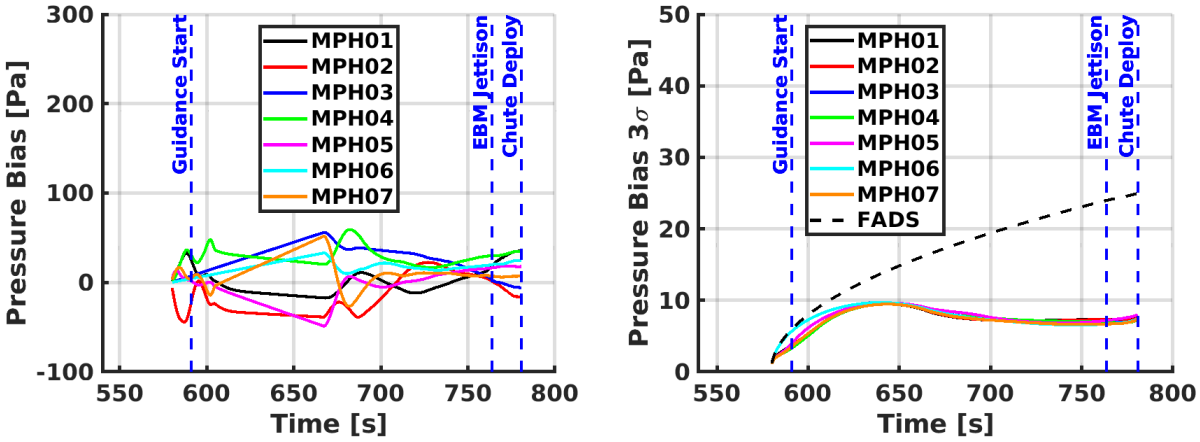

(a) Transducer bias.

(b) Transducer bias uncertainty.

Fig. 10 Reconstructed pressure measurement bias.

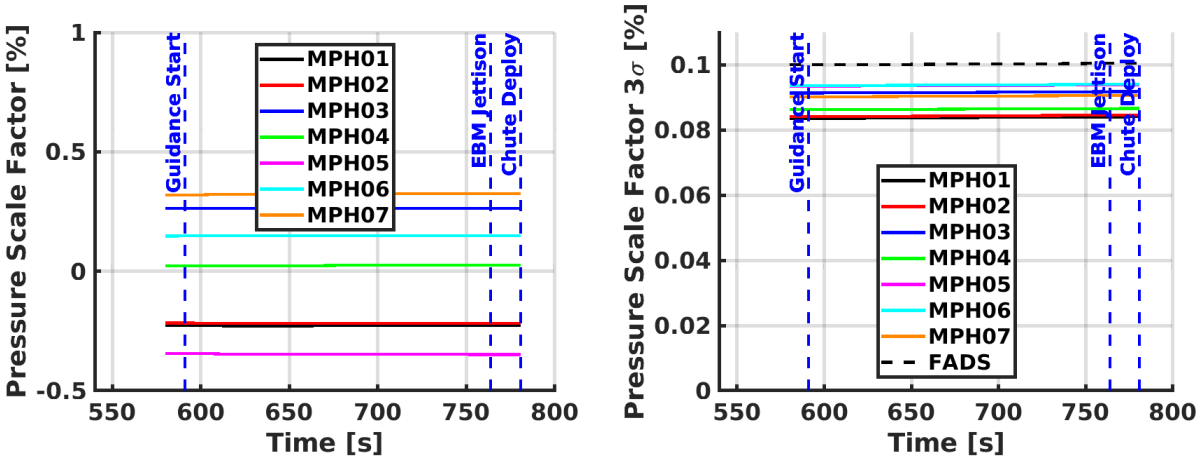

(a) Transducer scale factor.

(b) Transducer scale factor uncertainty

Fig. 11 Reconstructed pressure measurement scale factor.

The estimated aerodynamic parameters are listed in Table 2. Recall that these parameters are nondimensionalized inputs such that the mean value is zero and the $\pm 3\sigma$ error corresponds to ± 1. The estimated values from the filter are shown along with the corresponding 3σ uncertainties based on the state covariance estimate. The filter was able to converge on a reasonable set of aerodynamic parameters that are within the preflight 3σ uncertainty bounds. Note that the results in Table 2 include those for both the MSL and the Mars 2020 application. In each case, the uncertainties of the derived uncertainty parameters is similar between the two vehicles. However, not all of the estimated parameters are in agreement even though the two vehicles had the same nominal aeroshell shape. In particular, the axial force coefficient derived from the MSL data was higher than nominal while that derived from Mars 2020 was below nominal. These findings are consistent with the aerodynamic reconstruction based on FADS solutions [2, 4, 34]. Reconciling differences between the reconstructed aerodynamic parameters of the two entry capsules is for future work.

Table 2 Aerodynamic parameter estimates.

	MSL		Mars 2020	
Parameter	Estimate	3σ	Estimate	3σ
Hypersonic C_A Multiplier	0.5151	0.0655	-0.7193	0.0764
Supersonic C_A Multiplier	0.3321	0.0610	-0.1964	0.0665
Hypersonic C_N Adder	-0.3641	0.4991	-0.3245	0.5067
Hypersonic C_N Multiplier	0.2786	0.8713	0.1778	0.8745
Supersonic C_N Adder	-0.2633	0.6098	-0.1504	0.6334
Supersonic C_N Multiplier	0.1406	0.9075	0.0833	0.9121
Hypersonic C_Y Adder	0.0413	0.1372	-0.0853	0.1813
Supersonic C_Y Adder	0.1312	0.4940	0.0399	0.5505
Hypersonic C_m Adder	-0.0097	0.0246	0.0891	0.0243
Hypersonic C_m Multiplier	0.2421	0.4550	-0.2439	0.7026
Supersonic C_m Adder	-0.0258	0.1059	0.1554	0.0995
Supersonic C_m Multiplier	-0.3848	0.8418	-0.1416	0.8958
Hypersonic C_n Adder	-0.0206	0.0293	0.0637	0.0335
Supersonic C_n Adder	-0.1223	0.0797	-0.1169	0.0747

IV. Conclusions

A hybrid estimator for simultaneous processing flush air data and synthetic air data sensing measurements for entry vehicle atmosphere estimation is developed. The approach uses a Kalman-Schmidt Filter and Rauch-Tung-Streibel Smoother for blending flush air data pressure measurements with an aerodynamic model of the entry capsule to produce estimates of the freestream atmospheric conditions along the trajectory. The hybrid approach combining both sets of measurement data enables the estimation of systematic error parameters in the form of bias and scale factors. Sample results indicate that the hybrid filter produces estimates of the atmospheric-relative trajectory that have lower uncertainties. The hybrid filter approach is expected to be useful for future atmospheric entry trajectory reconstruction problems where flush air data measurements are available.

Acknowledgments

This work was funded under Technology Engineering and Aerospace Mission Support 3 (TEAMS3) contract number 80LARC17C0003 with NASA Langley Research Center.

References

[1] Kutty, P., "Reconstruction and Uncertainty Quantification of Entry, Descent, and Landing Trajectories using Vehicle Aerodynamics," M. S. Thesis, School of Aerospace Engineering, Georgia Institute of Technology, Atlanta, GA, May 2014.

[2] Karlgaard, C. D., Kutty, P., Schoenenberger, M., Munk, M. M., Little, A., Kuhl, C. A., and Shidner, J., "Mars Science Laboratory Entry Atmospheric Data System Trajectory and Atmosphere Reconstruction," *Journal of Spacecraft and Rockets*, Vol. 51, No. 4, 2014, pp. 1029–1047. https://doi.org/10.2514/1.A32770.

[3] Karlgaard, C. D., Kutty, P. M., and Schoenenberger, M., "Coupled Inertial Navigation and Flush Air Data Sensing Algorithm for Atmosphere Estimation," *Journal of Spacecraft and Rockets*, Vol. 54, No. 1, 2017, pp. 128-140. https://doi.org/10.2514/1.A33331.

[4] Karlgaard, C. D., Schoenenberger, M., Dutta, S., and Way, D. W., "Mars Entry, Descent, and Landing Instrumentation 2 Trajectory and Atmosphere Reconstruction," *Journal of Spacecraft and Rockets*, Vol. 60, No. 1, 2023, pp. 199-214. https://doi.org/10.2514/1.A35440.

[5] Whitmore, S. A., Davis, R. J., and Fife, J. M., "In-Flight Demonstration of a Real-Time Flush Airdata Sensing System," *Journal of Aircraft*, Vol. 33, No. 5, 1998, pp. 970–977. https://doi.org/10.2514/3.47043.

[6] Baumann, E., Pahle, J. W., Davis, M. C., and White, J. T., "X-43A Flush Airdata Sensing System Flight-Test Results," *Journal of Spacecraft and Rockets*, Vol. 47, No. 1, 2010, pp. 48–61. https://doi.org/10.2514/1.41163.

[7] Takahashi, H., Hasegawa, S. and Tani, K., "Simplified Real-Time Flush Air-Data Sensing System for Sharp-Nosed Hypersonic Vehicles," *Journal of Spacecraft and Rockets*, Vol. 60, No. 5, 2023, pp. 1437–1447. https://doi.org/10.2514/1.A35634.

[8] Lugo, R. A., Karlgaard, C. D., Powell, R. W., and Dwyer-Cianciolo, A, "Integrated Flush Air Data Sensing System Modeling for Planetary Entry Guidance with Direct Force Control," AIAA Paper 2019-0663, January 2019. https://doi.org/10.2514/6.2019-0663.

[9] Craft, K. J. and DeMars, K. J., "Navigation Performance of Air Data Systems for Atmospheric Entry and Descent," AIAA Paper 2022–1218, January 2022. https://doi.org/10.2514/6.2022-1218.

[10] Fife, W. N. and DeMars, K. J., "Error State Filtering for Atmospheric Landing Using Air Data Systems," AIAA Paper 2023–2324, January 2023. https://doi.org/10.2514/6.2023-2324.

[11] Whitmore, S., Moes, T., and Leondes, C., "Failure Detection and Fault Management Techniques for Flush Airdata Sensing Systems," AIAA Paper 92-0263, January 1992. https://doi.org/10.2514/6.1992-263.

[12] Hansen, S. and Blanke, M., "Diagnosis of Airspeed Measurement Faults for Unmanned Aerial Vehicles," *IEEE Transactions on Aerospace and Electronic Systems*, Vol. 50, No. 1, 2014, pp. 224-239. https://doi.org/10.1109/TAES.2013.120420.

[13] Guo, D., Zhong, M., and Zhou, D., "Multisensor Data-Fusion-Based Approach to Airspeed Measurement Fault Detection for Unmanned Aerial Vehicles," *IEEE Transactions on Instrumentation and Measurement*, Vol. 67, No. 2, 2018, pp. 317-327. https://doi.org/10.1109/TIM.2017.2735663.

[14] Fravolini, M. L., del Core, G., Papa, U., Valigi, P., nd Napolitano, M. R., "Data-Driven Schemes for Robust Fault Detection of Air Data System Sensors," *IEEE Transactions on Control Systems Technology*, Vol. 27, No. 1, 2019, pp. 234-248. https://doi.org/10.1109/TCST.2017.2758345.

[15] Wan, Q., Zhang, M., Zuo, G., and Xie, T., "Fault-tolerant FADS System Development for a Hypersonic Vehicle via Neural Network Algorithms," *Theoretical and Applied Mechanics Letters*, Vol. 13, 202. https://doi.org/10.1016/j.taml.2023.100464

[16] Lie, F., and Gebre-Egziabher, D., "Synthetic Air Data System," *Journal of Aircraft*, Vol. 50, No. 4, 2013, pp. 1234–1249. https://doi.org/10.2514/1.C032177.

[17] de Morais Veras, V. L. and Goes, L. C. S., "A Synthetic Airspeed Algorithm in Frequency Domain," AIAA Paper 2023–4457, June 2023. https://doi.org/10.2514/6.2023-4457.

[18] Karali, H., Uzun, M., Yuksek, B., and Inalhan, G., "Data-driven Synthetic Air Data Estimation System Development for a Fighter Aircraft," AIAA Paper 2023–3439, June 2023. https://doi.org/10.2514/6.2023-3439.

[19] Karlgaard, C., D. and Schoenenberger, M., "Planetary Probe Entry Atmosphere Estimation Using Synthetic Air Data System," *Journal of Spacecraft and Rockets*, Vol. 55, No. 3, 2018, pp. 599-610. https://doi.org/10.2514/1.A34115.

[20] Karlgaard, C. D., "Synthetic Air Data Sensing Applied to Phoenix and InSight Entry Atmosphere Reconstruction," *Journal of Spacecraft and Rockets*, Vol. 59, No. 4, 2022, pp. 1369-1401. https://doi.org/10.2514/1.A35082.

[21] Tian, P., Chao, H., Flanagan, H. P., Hagerott, S. G., and Gu, Y., "Design and Evaluation of UAV Flow Angle Estimation Filters," *IEEE Transactions on Aerospace and Electronic Systems*, Vol. 55, No. 1, 2019, pp. 371–383. https://doi.org/10.1109/TAES.2018.2852359.

[22] Sun, J., Li, B., Wen, C-Y. and Chen, C-K., "Model-Aided Wind Estimation Method for a Tail-Sitter Aircraft," *IEEE Transactions on Aerospace and Electronic Systems*, Vol. 56, No. 2, 2020, pp. 1262–1278. https://doi.org/10.1109/TAES.2019.2929379.

[23] Wenz, A. and Johansen, T. A., "Moving Horizon Estimation of Air Data Parameters for UAVs," *IEEE Transactions on Aerospace and Electronic Systems*, Vol. 56, No. 3, 2020, pp. 2101–2121. https://doi.org/10.1109/TAES.2019.2946677.

[24] Youn, W., Choi, H. S., Ryu, H., Kim, S., and Rhudy, M., "Model-Aided State Estimation of HALE UAV with Synthetic AOA/SSA for Analytical Redundancy," *IEEE Sensors Journal*, Vol. 20, No. 14, 2020, pp. 7929–7940. https://doi.org/10.1109/JSEN.2020.2981042.

[25] Lim, H., Ryu, H., Rhudy, M., Lee, D., Jang, D., Lee, C., Park, Y., Youn, W., and Myung, H., "Deep Learning-Aided Synthetic Airspeed Estimation of UAVs for Analytical Redundancy with a Temporal Convolutional Network," *IEEE Robotics and Automation Letters*, Vol. 7, No. 1, 2022, pp. 17–24. https://doi.org/10.1109/LRA.2021.3117021.

[26] Brown, E. N., Friehe, C. A., and Lenschow, D. H., "The Use of Pressure Fluctuations on the Nose of an Aircraft for Measuring Air Motion," *Journal of Climate and Applied Meteorology*, Vol. 22, No. 1, 1983, pp. 171–180. https://doi.org/10.1175/1520-0450(1983)022<3C0171:TUOPFO>3E2.0.CO;2

[27] Pruett, C. D., Wolf, H., Heck, M. L., and Siemers, P. M., "Innovative Air Data System for the Space Shuttle Orbiter," *Journal of Spacecraft and Rockets*, Vol. 20, No. 1, 1983, pp. 61–69. https://doi.org/10.2514/3.28357

[28] Cobleigh, B. R., Whitmore, S. A., Haering, E. A., Jr., Borrer, J., and Roback, V. E., "Flush Airdata Sensing (FADS) System Calibration Procedures and Results for Blunt Forebodies," NASA TP-1999-209012, November 1999.

[29] Johnston, I. A., Jacobs, P. A., and Shimoda, T., "Flush Air Data System Calibration Using Numerical Simulation," *Journal of Spacecraft and Rockets*, Vol. 35, No. 6, 1998, pp. 812–820. https://doi.org/10.2514/2.3404.

[30] Van Hove, B., Karatekin, Ö Schleukter, T., and Gülhan, A., "ExoMars Flush Air Data System: Entry Simulation and Atmospheric Reconstruction Method," *Journal of Spacecraft and Rockets*, Vol. 56, No. 4, 2019, pp. 1205–1220. https://doi.org/10.2514/1.A34187.

[31] Schmidt, S. F., "Application of State-Space Methods to Navigation Problems," *Advances in Control Systems*, Vol. 3, 1966, pp. 293–340. doi: 10.1016/B978-1-4831-6716-9.50011-4.

[32] Rauch, H. E., Tung, F., and Striebel, C. T., "Maximum Likelihood Estimates of Linear Dynamic Systems," *AIAA Journal*, Vol. 3, No. 8, 1965, pp. 1445–1450. doi: 10.2514/3.3166.

[33] Nelessen, A., Sackier, C., Clack, I., Brugarolas, P., Villar, G., Chen, A., Stehura, A., Otero, R., Stilley, E., Way, D., Edquist, K., Mohan, S., Giovingo, C., and Lefland, M., "Mars 2020 Entry, Descent, and Landing System Overview," IEEE Aerospace Conference, March 2019. https://doi.org/10.1109/AERO.2019.8742167.

[34] Schoenenberger, M., Van Norman, J., Karlgaard, C., Kutty, P., and Way, D.,"Assessment of the Reconstructed Aerodynamics of the Mars Science Laboratory Entry Vehicle," *Journal of Spacecraft and Rockets*, Vol. 51, No. 4, 2014, pp. 1076–1093. https://doi.org/10.2514/1.A32794.

[35] Karlgaard, C. D., Schoenenberger, M., and Van Norman, J., "Base Drag Model Derived from Mars 2020 Backshell Pressure Measurements," *Journal of Spacecraft and Rockets*, https://doi.org/10.2514/1.A35774

[36] Dutta, S., Karlgaard, C. D., Kass, D., Villar, G., and Mischna, M., "Post-flight Analysis of Atmospheric Properties from Mars 2020 Entry, Descent, and Landing," *Journal of Spacecraft and Rockets*, Vol. 60, 2023. https://doi.org/10.2514/1.A35561.

[37] Mischna, M., Villar, G., Kass, D., Dutta, S., Rafkin, S., Tyler, D., Barnes, J., Cantor, B., Lewis, S., Hinson, D., Pla-Garcia, J., Kleinbohl, A., and Karlgaard, C., "Pre- and Post-Entry, Descent and Landing Assessment of the Martian Atmosphere for the Mars 2020 Rover," *The Planetary Science Journal*, Vol. 3, No. 147, June 2022, pp. 1–28. https://doi.org/10.3847/PSJ/ac7148.

[38] Karlgaard, C. D., Van Norman, J., Siemers, P. M., Schoenenberger, M., and Munk, M. M., "Mars Entry Atmospheric Data System Modeling, Calibration, and Error Analysis," NASA TM-2014-218535, October 2014.

[39] Karlgaard, C. D., Trombetta, D. R., Wilson, M., Petzar, P., Jackson, A., Ragin, M., Schoenenberger, M., and Van Norman, J., "Mars Entry, Descent, and Landing Instrumentation 2 Entry Air Data System Modeling, Calibration, and Performance Analysis," NASA TM-20220003550, March 2022.